

## Article

# Diagenetic Impact on High-Pressure High-Temperature Reservoirs in Deep-Water Submarine Fan Sandstone of Qiongdongnan Basin, South China Sea

Lin Hu <sup>1</sup>, Wei Luo <sup>1</sup> and Benben Ma <sup>2,\*</sup><sup>1</sup> Hainan Branch of CNOOC Limited, Haikou 570100, China<sup>2</sup> Key Laboratory of Tectonics and Petroleum Resources, China University of Geosciences, Ministry of Education, Wuhan 430074, China

\* Correspondence: mabenben@cug.edu.cn

**Abstract:** The diagenetic evolution of sandstone is very complicated under the conditions of high temperatures and pressures in deep-water, deep-buried regimes, which have great influence on reservoir quality. This study investigates the typical reservoir target of Neogene deep-water, submarine-fan sandstones under high-temperature, high-pressure regimes in the Qiongdongnan Basin, South China Sea. Utilizing a thin section, scanning electron microscope (SEM), mineral geochemistry combined with burial history evolution, complex diagenetic events, and main controlling factors of the sandstone in the Neogene Meishan Formation were determined. The results show that the evolution of sandstone reservoirs is initially controlled by depositional framework compositions and subsequently modified by eogenetic and mesogenetic alterations during progressive burial. Eogenetic alterations mainly include the following: (1) mechanical compaction; (2) dissolution of feldspar; (3) low-Fe calcite cementation. Mesogenetic events were identified as the following: (1) dissolution of feldspar; (2) ferroan calcite and ankerite formation; (3) precipitation of quartz and clay mineral. Mechanical compaction is greatly influenced by the original depositional framework composition, and sandstone samples enriched in high contents of detrital clay matrix always experienced extensive mechanical compaction. Different phases of carbonate cement during different diagenetic regimes lead to continuous destruction on reservoir porosity. The dissolution of unstable feldspar minerals during eogenetic and mesogenetic environments leads to the development of secondary porosities and would enhance the quality of the reservoir. Overpressure formation is pervasively developed owing to early disequilibrium compaction and subsequent natural gas charging. Only well-sorted sandstones with low contents of detrital clay matrix could resist early mechanical compaction, lead to ample residual original porosities, and then undergo extensive mineral dissolution to generate sufficient secondary porosities. Subsequently, these porosities would be effectively protected by overpressure formation. Poor-sorted sandstones with high contents of detrital clay matrix would experience strong mechanical compaction and extensive destruction of original porosities. Thus, these sandstones are difficult to have significant dissolution and are unable to be effectively protected by overpressure formation. Therefore, the interplay between the original framework composition and the corresponding diagenetic pathways coupled with overpressure formation would result in strong reservoir heterogeneity for the deep-buried sandstones during progressive burial.



**Citation:** Hu, L.; Luo, W.; Ma, B. Diagenetic Impact on High-Pressure High-Temperature Reservoirs in Deep-Water Submarine Fan Sandstone of Qiongdongnan Basin, South China Sea. *Minerals* **2024**, *14*, 361. <https://doi.org/10.3390/min14040361>

Academic Editors: Daniel Rodrigues do Nascimento Junior, Ana Clara Braga de Souza and Thomas Gentzis

Received: 3 February 2024

Revised: 1 March 2024

Accepted: 6 March 2024

Published: 29 March 2024



**Copyright:** © 2024 by the authors. Licensee MDPI, Basel, Switzerland. This article is an open access article distributed under the terms and conditions of the Creative Commons Attribution (CC BY) license (<https://creativecommons.org/licenses/by/4.0/>).

**Keywords:** depositional heterogeneities; deep-marine fan deposition; petroleum exploration; diagenetic history; reservoir quality; Neogene; Qiongdongnan Basin

## 1. Introduction

As hydrocarbon exploration moves forward in sedimentary basins, sufficiently high reservoir properties are being increasingly explored in the deeply buried sandstones, which would provide economic support for commercial development [1]. Hydrocarbon

exploration has gradually expanded into marine deep-water environments [2], Deep-water sandstones represent crucial reservoirs of these resources under high-temperature and high-pressure (HTHP) conditions [3]. However, the fundamental mechanisms of deep-buried, deep-water sandstone diagenesis and the associated reservoir quality under extreme HTHP regimes remain poorly understood, which might lead to making an inaccurate prediction of these sandstones of similar origins [4]. Temperature and pressure are closely related to hydrocarbon exploration and have significant effects on reservoir diagenesis [3]. With the increase in temperature, the mechanical compaction of sandstone will also increase. High temperature also has a certain effect on the dissolution of minerals. The solubility of minerals increases with the increase in temperature. Temperature is uncertain for mineral dissolution, and it will inhibit the dissolution of some minerals under high-temperature conditions. Sandstone reservoirs affected by high temperature result in many diagenetic products and strong homogeneity [5]. Overpressure has many effects on the diagenesis of sandstone reservoir. Overpressure can support the overlying rock mass to reduce the effective stress in the formation, slow down the compaction of the formation, and effectively inhibit the pressure dissolution, and play a certain role in protecting the primary pores [6,7]. Overpressure can prevent the migration of diagenetic fluid, effectively slow down or inhibit the cementation, and protect the pore structure [8,9]. However, the influence of the overpressure formation mechanism and time on reservoir quality are still unclear.

A submarine fan is defined as a kind of fan-shaped or conical sedimentary body, which transports terrigenous debris to the seafloor through the submarine canyon in the front of the continental slope [10–12]. The submarine-fan sandstone reservoirs deposited in a deep water environment has strong heterogeneity owing to variable depositional textures and compositions among different lithofacies [13,14]. At present, the study on the quality difference of submarine fan reservoirs under the influence of sedimentary diagenesis and its main controlling factors is still relatively weak. Therefore, in-depth study of the sedimentary characteristics, sedimentary systems, and sedimentary models of typical deep-water submarine fans in this area is of great significance for analyzing the controlling factors of deep-water submarine fans and predicting high-quality reservoirs, and is also helpful to guide the exploration and development of deep-water oil and gas fields in this area. At the same time, how to effectively develop submarine fan reservoir under high temperatures and high pressures has become an urgent problem and research focus.

The Ledong–Lingshui Sag, located in the Qiongdongnan Basin in South China Sea, is an archetypal site specific to a Neogene submarine fan system. With typical high-temperature overpressure characteristics, it is an important exploration area for increasing natural gas production in Qiongdongnan Basin (Figure 1) [5,15]. The submarine fan of the Neogene Meishan Formation is the main reservoir in the studied area, and reservoir quality is jointly affected by deposition and diagenesis. The study of deep-buried sandstones within this unique geologic setting offers an opportunity to better understand the diagenetic processes and impacts on reservoir quality evolution when subjected to extreme HTHP conditions. In this paper, several research questions related to diagenesis of deeply buried sandstones are addressed including the following: (1) how the original depositional framework composition of sandstones influenced their later diagenetic history; (2) clarifying the formation mechanism and time of overpressure and revealing the influence on the pore structure of reservoir; (3) evaluating the influence of diagenetic modifications on the reservoir quality of deep-water, deep-buried submarine fan sandstones.

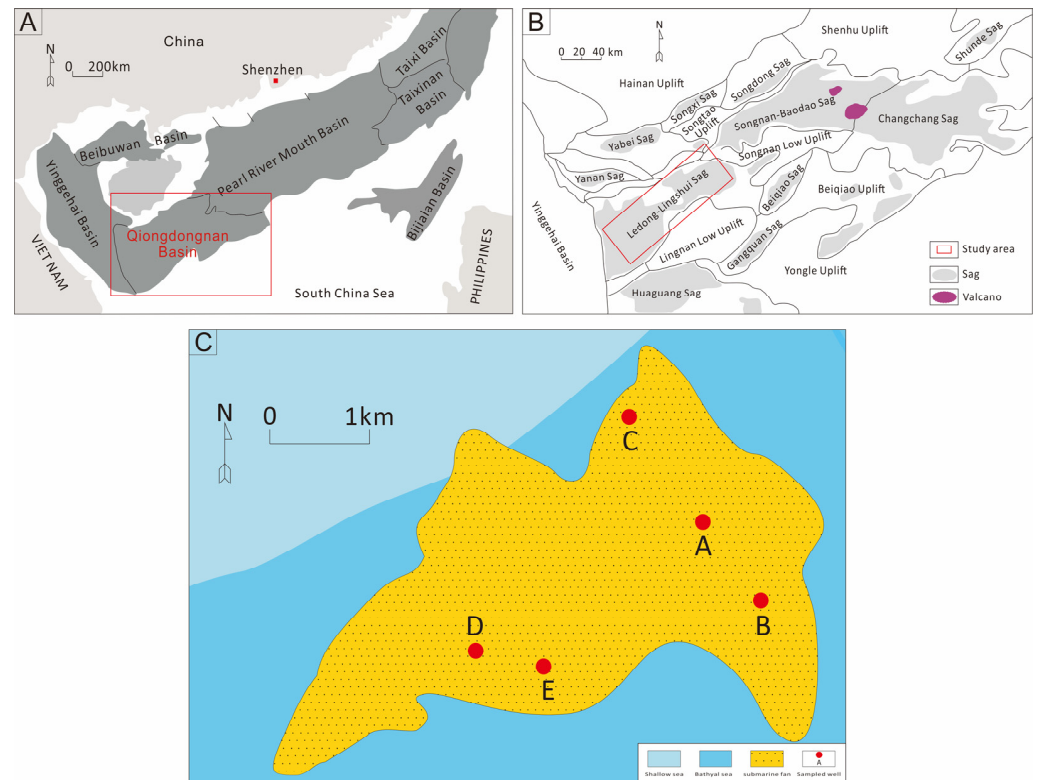


**Figure 1.** (A,B) Locality map showing major tectonic units in the Qiongdongnan Basin and location of the study area (adopted from [16]). (C) Map of depositional facies with well locations for the  $N_{1m}$  interval in the LS13 gas field, Ledong–Lingshui Sag.

## 2. Geological Setting

### 2.1. Tectonics

The Qiongdongnan Basin in South China Sea is one of the most important deep-water oil and gas exploration areas in China (Figure 1A). In the past decade, oil and gas exploration in the deep water area of the basin mainly concentrated in the Meishan Formation reservoir, with a burial depth of 3000–4000 m [3,5,17]. Qiongdongnan Basin has a “multi-depression and multi-uplift” tectonic pattern, which is divided into four tectonic units from north to south: northern depression, central uplift, central depression, and southern uplift. Among them, the deep water area has a water depth greater than 300 m is  $5.3 \times 10^4 \text{ km}^2$  [18], which mainly includes the Lingnan low uplift, Songnan low uplift, Ledong sag, Lingshui Sag, Songnan–Baodao Sag, Changchang Sag, and other secondary structural units (Figure 1B). Ledong–Lingshui Sag is located in the western part of the central depression of the basin, separated from Songnan–Baodao Sag and Changchang Sag by the Songnan Low uplift in the east, separated from Huaguang Sag by the Lingnan Low uplift in the south, bounded by the Ya Nan Low uplift and Lingshui low uplift in the north, and the Zhongjian uplift in the west (Figure 1B).

### 2.2. Stratigraphy and Depositional Facies

Figure 2 displays the sedimentary fill sequence of the Qiongdongnan Basin, which mainly consists of Paleogene, Neogene, and Quaternary formations. The stratigraphic units, from bottom to top, are the Eocene ( $E_2$ ), the Early Oligocene ( $E_{3y}$ ), the Late Oligocene ( $E_{3l}$ ), the Early Miocene ( $N_{1s}$ ), the Middle Miocene ( $N_{1m}$ ), the Late Miocene ( $N_{1h}$ ), the Pliocene ( $N_{2y}$ ), and the Quaternary ( $Q_1$ ). In the Paleogene system, the Eocene primarily consists of terrestrial sedimentation, which is a product of the early stage of rifting. The overall basin, controlled by faulting, exhibits a “multi-concave and multi-convex” characteristic [19]. The Yacheng formation is the sedimentation product of the late rifting phase, the lower part of the Lingshui formation is a marine–terrestrial transitional phase of sedimentation,

and the middle-upper parts are primarily marine sedimentation [20,21]. In the Neogene system, the Sanya formation is divided into upper and lower segments, representing the initial filling stage after the rifting of the basin. The Meishan formation (age: 15.5–10.5 Ma) is predominantly shallow gray–gray sandstone and mudstone, with thin layers of silty sandstone and fine sandstone, constituting a semi-deep to deep marine sediment system overall [19,22,23] (Figure 2). The Ledong–Lingshui depression is primarily composed of three sets of hydrocarbon source rocks from the Eocene lacustrine facies, Oligocene transitional facies between the marine and terrestrial environments, and Miocene bathyal to abyssal facies [24]. The total organic carbon (TOC) content of the source rocks mostly ranges from 0.5% to 1.5%. The organic matter is predominantly a humic-type kerogen. This set of source rocks is widely distributed with a large scale [25].

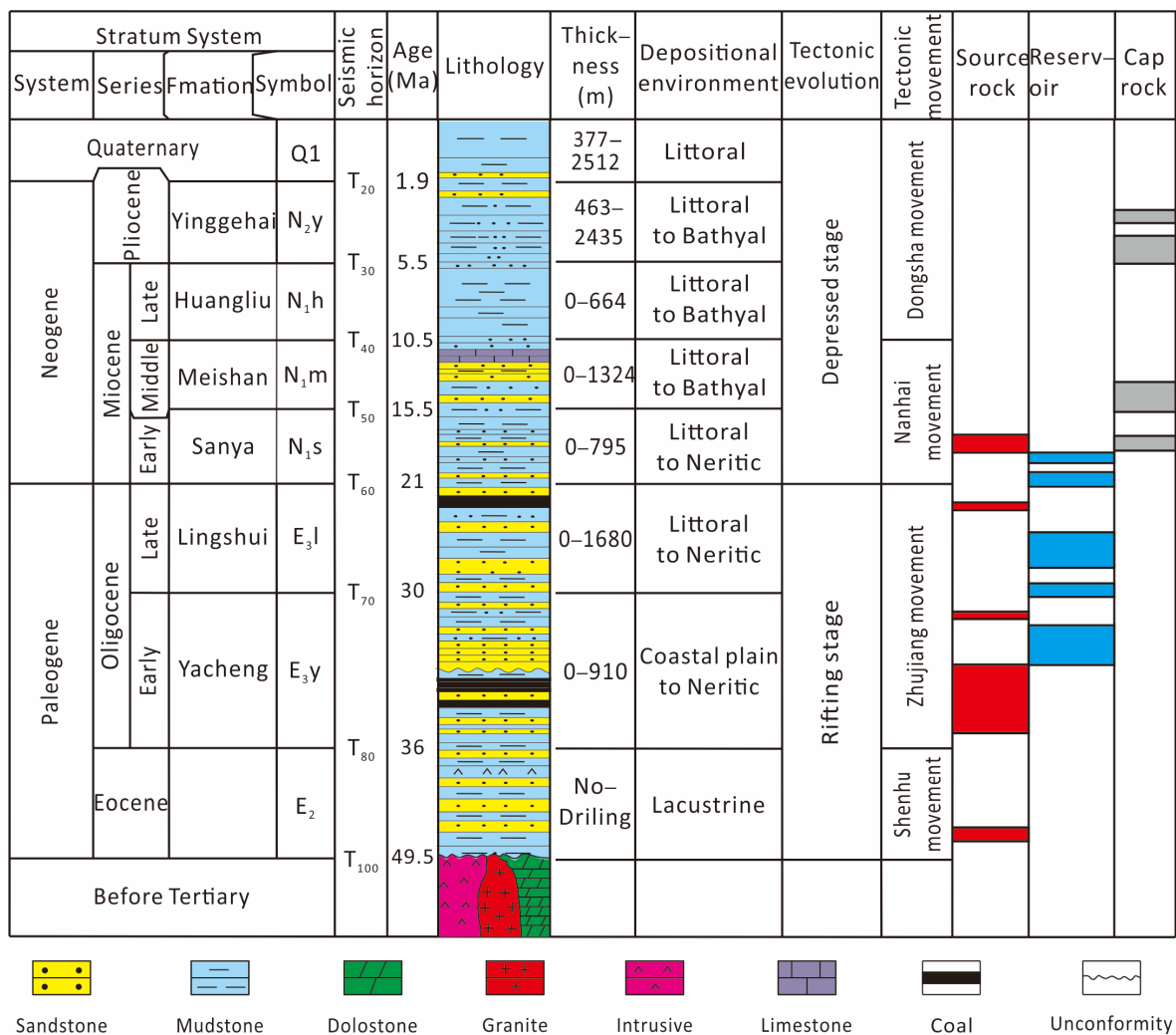


Figure 2. Stratigraphy, tectonic evolution, and key elements of petroleum system in the Ledong–Lingshui Sag (adopted from [16]).

The submarine fan sedimentary complexes in the Ledong–Lingshui Depression exhibit various styles and planar forms [24], primarily influenced by the sand–mud ratio of sediments, the paleogeomorphology of the seabed, and the duration of the marginal delta [22]. Based on their development location and sedimentary body morphology, the submarine fans can be classified into three types. The channelized submarine fan develops in steep slope areas, mainly in the early lowstand system tract. The basin-floor fan-type submarine fan develops at the foot of the slope and in the depression center, also mainly in

the lowstand system tract. The bottom-current reformed submarine fan develops in the central position of the depression and is a product of the highstand system tract [26].

### 3. Materials and Methods

A total of 65 core samples from 4 boreholes were collected at the depths of 3200–3900 m in the N<sub>1</sub>m interval. A total of 84 polished thin sections were impregnated with blue epoxy under vacuum and stained with Alizarin red-S and potassium ferricyanide [27]. The percentage of debris grains, authigenic cementitious materials, and porosity is determined by counting 400 points per thin section [28].

The compositions of authigenic minerals and their spatial relationships were investigated in 5 sample chips that were carbon plated using a ZEISS EVO LS15 scanning electron microscope (SEM) equipped with a QUANTAX400 energy dispersive X-ray spectra (EDX) in the China University of Geosciences (Wuhan, China). The resolution reaches 1.3 nm and 1.0 nm with an accelerating voltage of 1 kV and 15 kV, respectively. The average resolution applied to the samples in this study is the  $\mu\text{m}$  scale.

A total of 17 carbonate-cemented core chips were ground into powdered samples used for stable carbon and oxygen isotopic measurements. The powdered samples (5 mg) were reacted with 100% ortho-phosphoric acid at 70 °C for approximately 8 h. Stable isotopic compositions of carbon and oxygen were determined based on calculating the CO<sub>2</sub> gas released from a reaction with the acids. The analysis was carried out on an isotope-ratio mass spectrometer (IRMS) in Key Laboratory of Tectonics and Petroleum Resources, China University of Geosciences (Wuhan, China). The measurements of carbon and oxygen isotopes were documented in standard delta notation as per mil (‰) deviations from Vienna Pee Dee Belemnite (VPDB).

DSTs from the Well A, Well B, and Well C mud weights, and well logs from the Well A and Well D were provided by the Haikou Branch of CNOOC to characterize the current formation pressures. In this study, we used the pressure coefficient (C<sub>p</sub>) method to depict the overpressure magnitude. The pressure coefficient refers to the ratio of the actual pore pressure to the corresponding calculated hydrostatic pressure at a given depth. Moreover, 114 core porosity and permeability data were collected from the Haikou Branch of CNOOC.

## 4. Results

### 4.1. Rock Petrology

The studied sandstone is mainly composed of sublitharenite, followed by minor feldspathic litharenite (Figure 3A; [29]). Based on point-count data, detrital quartz is the most abundant framework grain with content ranges between 69.2% and 85% (average 78.2%). Detrital quartz is predominantly monocrystalline. The rock fragments are the subordinate framework constituents (9.00% to 23.20%, average 13.80%). The rock fragments are mainly composed of metamorphic rock (2.60%–11.50%, average 8.90%), sedimentary rock (0.10%–2.80%, average 2.00%), and volcanic rock (0.00%–1.20%, average 0.40%) (Figure 3B). Feldspar is the least common framework grain, making up about 5.00% to 13.00% (average 8.10%) of the composition. K-feldspar (4.00%–12.00%, average 7.00%) is more abundant than plagioclase (less than 1.00%). The pore-filling materials mainly include detrital clay matrix and diagenetic cement. Detrital clay matrix constitutes the highest proportion of the pore-filling materials (0.10%–43.00%, average 10.90%). The cements are mainly composed of carbonate (0.10%–22.00%, average 5.70%), authigenic glauconite (0.50%–13.00%, average 4.30%), and quartz cement (0.10%–0.90%, average 0.50%) (Figure 3C).

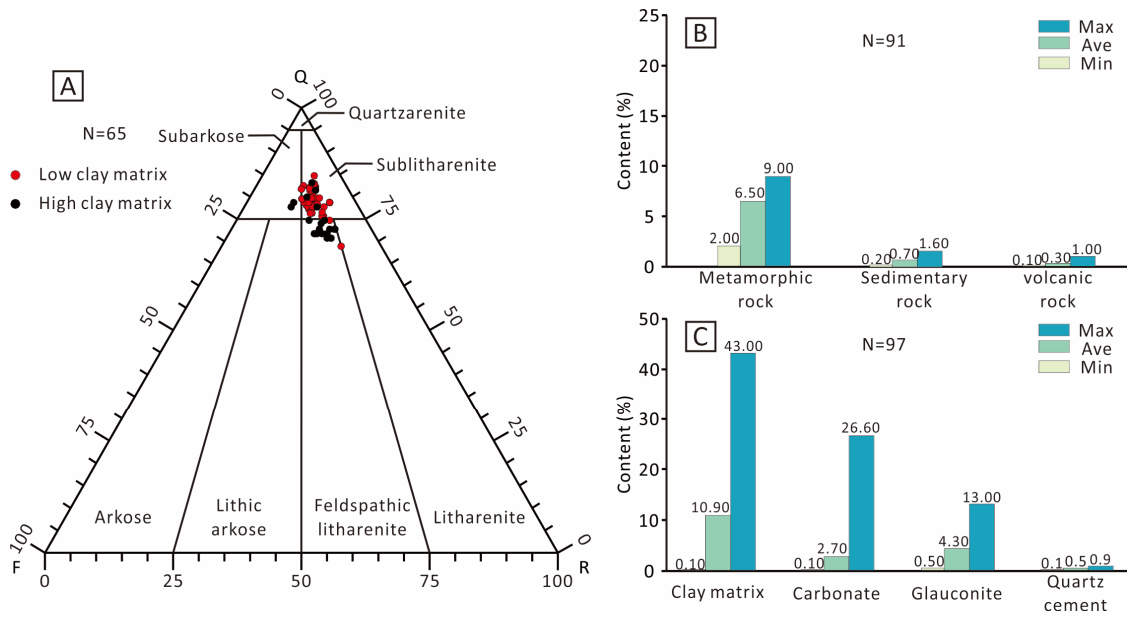


**Figure 3.** (A) QFR detrital compositions of sandstones of the Meishan Formation in the Qiongdongnan Basin plotted on a ternary diagram after Folk (1980). (B) Histogram of rock fragments in the N1m sandstones. (C) Histogram of filler component in the N1m sandstones.

4.2. Porosity and Permeability

A relatively good linear correlation ( $R^2 = 0.9006$ ) occurs between the core porosity and permeability in the N<sub>1</sub>m sandstones (Figure 4A). The core porosity ranges from 8.37% to 26.24% with an average of 19.14% (Figure 4B). The core permeability varies from 0.03 to 26.90 × mD (average 4.09 × mD) (Figure 4C). Abnormally high zones of porosity and permeability are developed at depths of 3700.00–3900.00 m (Figure 5A,B).

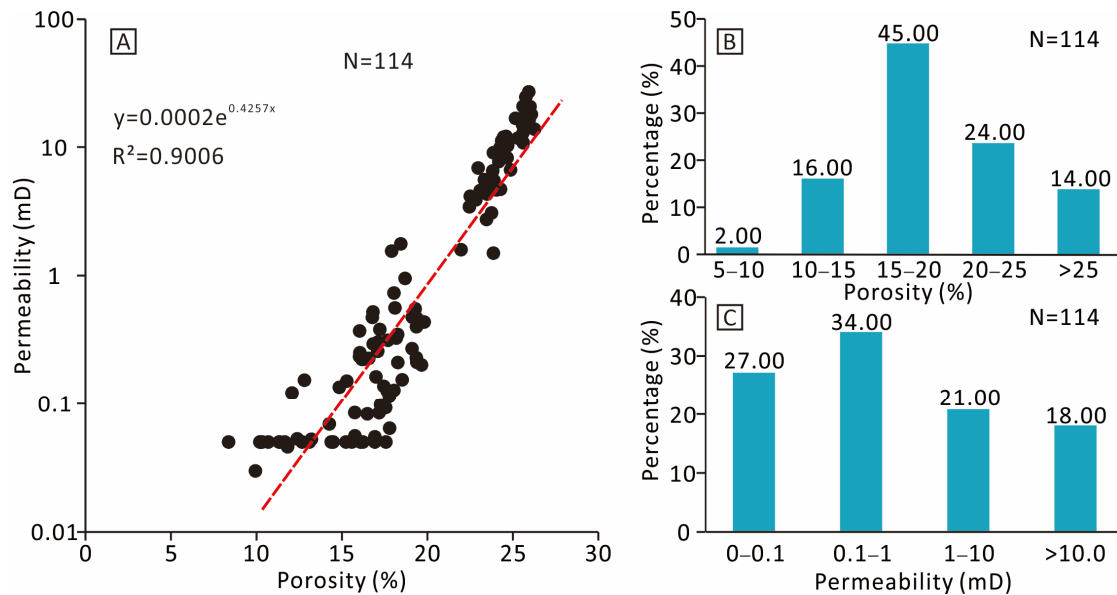


**Figure 4.** (A) Cross-plot of core porosity and permeability in the N1m sandstones. (B) Histograms showing core porosity variations in the N1m sandstones. (C) Histograms showing core permeability variations in the N1m sandstones.

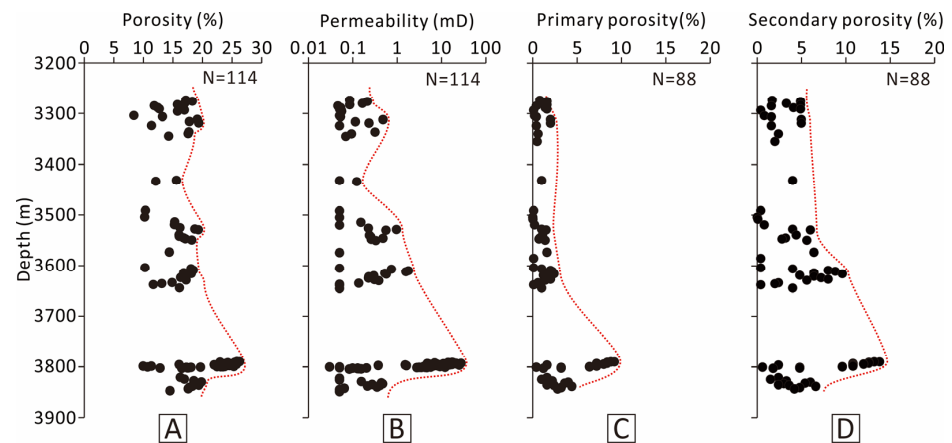


**Figure 5.** The vertical distribution characteristics of porosity (A), permeability (B), primary porosity (C), secondary porosity (D). The black dots represent the data points and the red lines represent the envelope.

#### 4.3. Diagenetic Products

Diagenetic products in the  $N_1m$  sandstones contain the following: (1) mechanical compaction, (2) cementation of carbonate and glauconite, (3) dissolution of feldspar, and (4) precipitation of clay minerals and authigenic quartz.

##### 4.3.1. Mechanical Compaction

Mechanical compaction in the  $N_1m$  interval evidenced by the deformation of mica plates and plastic grains (Figure 6A), the contact of intergranular lines to convex and convex contact (Figure 6B), rearrangement along a preferred direction (Figure 6C). Sandstone containing large amounts of detrital clay matrix exhibits extensive mechanical compaction and significant destruction of original intergranular porosity (Figure 6C). The sandstone with a low detrital clay matrix and high rigid grain and samples with extensive, early carbonate cementation display limited mechanical compaction (Figure 6D,E).

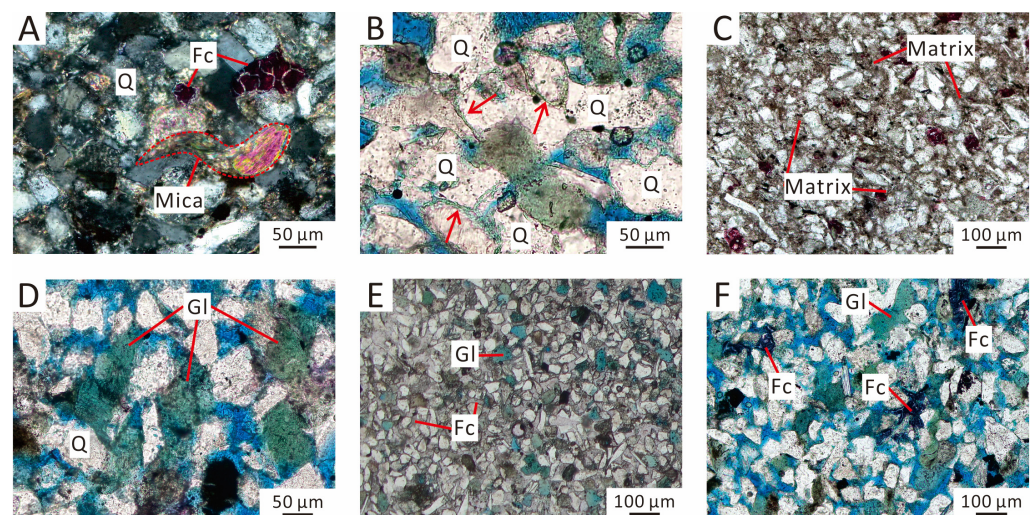


**Figure 6.** Photomicrographs and SEM images showing the features of the Meishan Formation. (A) Deformed micas in the  $N_1m$  sandstones, Well A, 3630 m. (B) Grains point contact to line contact, Well B, 3800.78 m. (C) Mechanical compaction is characterized by high matrix content and close contact of grains, Well A, 3605 m. (D) Glauconite fills the pores, Well B, 3791.74 m. (E) Ferroan calcite cements with low abundances of Fe is filled in intergranular pores, Well B, 3801.84 m. (F) Ferroan calcite cements with high abundances of Fe are filled in intergranular pores, Well B, 3795.9 m. Ca = Calcite, Fc = ferroan calcite, Q = Quartz, Gl = Glauconite.

#### 4.3.2. Glauconite

Thin sections demonstrate that glauconite mineral (0.50%–13.00%, average 4.30%; volume percent) is pervasively developed in the N<sub>1</sub>m sandstones (Figure 6D). The main characteristic of authigenic glauconite is the round or elliptic grains filled in the primary pores (Figure 6D–F).

#### 4.3.3. Carbonate Cements

Carbonate cement (0.10%–22.00%, average 5.70%; volume percent) is the most abundant diagenetic mineral and mainly consists of low-Fe calcite, ferroan calcite, and ankerite.

Calcite (0.10% to 20.00%, average 5.50%; volume percent) occurs as two forms in the studied sandstones: (1) poikilotopic light-red calcite with low-Fe contents (Figure 6E); (2) isolated purple ferroan calcite contents (Figure 6F). Ankerite (0.10% to 1.50%, average 0.30%; volume percent) typically occurs as isolated pore-filling cements in the form of euhedral rhombs (Figure 7A). Ferroan calcite and ankerite are spatially associated with glauconite minerals (Figures 6F and 7A).

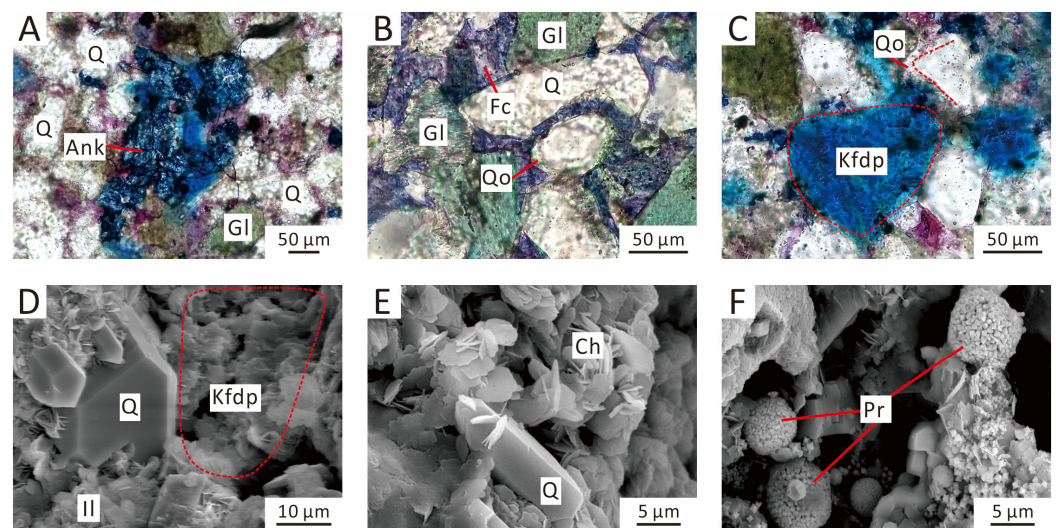


**Figure 7.** (A) Blocky ankerite, Well C, 3319 m. (B) Quartz overgrowth replaced by ferroan calcite cement. Well B, 3801.84 m. (C) Quartz overgrowths developed proximal to dissolved glauconite grain. Well LS13-2N-1, 3312 m. (D) Authigenic quartz and authigenic illite developed proximally to dissolved K-feldspar grain. Well B, 3792.39 m. (E) Authigenic chlorite and authigenic quartz. Well B, 3799.66 m. (F) SEM image of framboidal pyrite aggregates as pore-filling cement. Well B, 3792.33 m. Q = quartz, Ank = ankerite, Gl = glauconite, Fc = ferroan calcite, Qo = quartz overgrowth Kfdp = K-feldspar dissolution pores, Ill = illite, Ch = chlorite, Py = pyrite.

#### 4.3.4. Other Authigenic Minerals

Quartz cements, authigenic clays, and framboidal pyrite are observed as minor authigenic minerals in N<sub>1</sub>m sandstones (Figure 7B–F). Quartz cementation (less than 1.00%; volume percent) usually occurs in the form of syntaxial overgrowth on the surface of detrital quartz grains (Figure 7B,C), and SEM images show prismatic authigenic quartz filling the pore spaces (Figure 7D,E). In addition, quartz overgrowth by calcite replacement can be observed (Figure 8F). Authigenic clays (less than 0.50%; volume percent) include illite and chlorite; fibrous or flake authigenic illite mainly occurs in intergranular pores, and is occasionally present in feldspar dissolution pores (Figure 7D). Rosette-shaped, authigenic chlorite typically occur as pore-filling cements (Figure 7E). Authigenic illite and chlorite are spatially associated with authigenic quartz grains (Figure 7D,E). Framboidal pyrite (less than 1.00%; volume percent) occurs mainly as spheroidal aggregates in primary pores (Figure 7F).

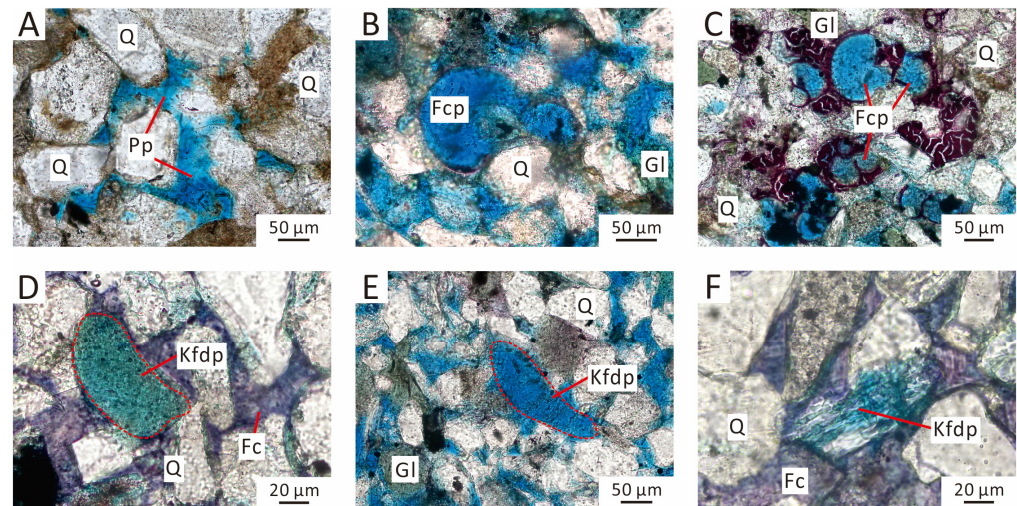


**Figure 8.** (A) Primary pores, Well LS13-2N-1, 3276 m. (B) Foraminifer chamber pores, Well B, 3792.24 m. (C) Foraminifer chamber pores, Well A, 3530 m. (D) K-feldspar solution pore, Well B, 3801.23 m. (E) Secondary pores related to K-feldspar dissolution, Well A, 3801.23 m. (F) Secondary pores related to K-feldspar dissolution along cleavage planes, Well B, 3801.84 m. Q = quartz, Pp = primary pores, Fcp = foraminifer chamber pores, Gl = glauconite, Kfdp = K-feldspar dissolution pores.

#### 4.3.5. Pore Types

The pore space is identified as two types: primary and secondary pores. Based on point counting data, total porosity ranges from 0.10% to 28.00% with an average of 9.50%. Primary pores include primary intergranular pores (Figure 8A) and foraminifer chamber pores (Figure 8B,C). The abundance of primary porosity is 0.10%–11.20%, with an average of 3.30% (Figure 5C). Chamber pores within unfilled foraminiferal shells is observed as typically primary pores (Figure 8B). Some chamber pores might be destroyed due to mechanical compaction or carbonate cementation (Figure 8C). The secondary pores are composed of a dissolution of feldspar and unstable framework grains (Figure 8D–F), and the abundance of secondary porosity is 0.1016.80% with an average of 6.10% (Figure 5D). The dissolution of feldspar grains is pervasively developed, and the dissolved feldspar grains are mostly K-feldspar (Figures 7D and 8D–F). The dissolution of feldspar is spatially related to quartz cements and clay mineral formation (Figure 7D).

#### 4.4. Pressure and Temperature

The formation pressure and pressure coefficient of the three boreholes in the LS13 area show that there is overpressure in the N<sub>1</sub>m sandstone reservoir. The distribution range of the formation pressure is 59.81–73.13 Mpa, with an average of 69.88 Mpa, and the corresponding pressure coefficient is 1.86–1.99, with an average of 1.96. The distribution of the formation temperature ranges from 138.1 to 152.05 °C, with an average of 148.48 °C (Table 1).

**Table 1.** Pressure, pressure coefficient, temperature, logging interpretation in the N1m interval.

Well	Depth (m)	Strata	Pressure (Mpa)	Pressure Coefficient	Temperature (°C)	Logging Interpretation
A	3607.80	N <sub>1</sub> m	69.48	1.98	148.42	Gas layer
A	3607.80	N <sub>1</sub> m	69.20	1.97	149.70	Gas layer
A	3611.00	N <sub>1</sub> m	69.59	1.98	147.99	Gas layer
A	3612.00	N <sub>1</sub> m	69.40	1.97	147.95	Gas layer
A	3625.00	N <sub>1</sub> m	69.16	1.96	149.10	Gas layer
B	3780.00	N <sub>1</sub> m	73.05	1.98	150.99	Gas layer
B	3786.00	N <sub>1</sub> m	73.10	1.98	150.31	Gas layer
B	3788.50	N <sub>1</sub> m	73.11	1.98	150.49	Gas layer

Table 1. Cont.

Well	Depth (m)	Strata	Pressure (Mpa)	Pressure Coefficient	Temperature (°C)	Logging Interpretation
B	3792.50	N <sub>1</sub> m	73.12	1.98	151.22	Gas layer
B	3794.00	N <sub>1</sub> m	73.12	1.98	151.88	Gas-water layer
B	3795.00	N <sub>1</sub> m	73.13	1.98	152.05	Gas-water layer
C	3309.01	N <sub>1</sub> m	59.91	1.86	138.62	Gas-water layer
C	3309.99	N <sub>1</sub> m	59.81	1.86	138.10	Gas-water layer

4.5. Stable Isotopic Composition

Low-Fe calcite cements are characterized by relatively high  $\delta^{13}C_{PDB}$  values ( $-2.69\text{‰}$  to  $-0.55\text{‰}$ ) and  $\delta^{18}O_{PDB}$  values ( $-9.22\text{‰}$  to  $-0.55\text{‰}$ ) (Figure 9 and Table 2).

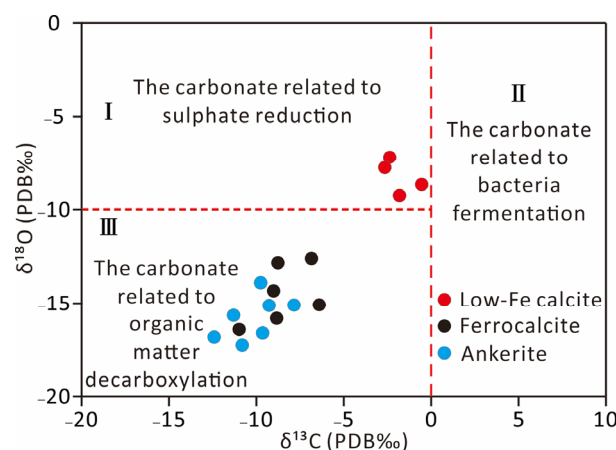


Figure 9. Cross-plot of stable carbon and oxygen isotopic compositions of different types of carbonate cements.

Table 2. Oxygen and carbon isotopic compositions and calculated precipitation temperatures of carbonate cements in the N<sub>1</sub>m interval.

Well	Depth (m)	Carbonate Cement	$\delta^{13}C$ (‰PDB)	$\delta^{18}O$ (‰PDB)	T-Precip. (°C)	
					$\delta^{18}O_{water}$ (‰) = 0‰	$\delta^{18}O_{water}$ (‰) = 4‰
B	3800.16	Low-Fe calcite	-2.36	-7.23	54.09	
B	3801.84	Low-Fe calcite	-2.70	-7.75	57.25	
B	3797.18	Low-Fe calcite	-1.81	-9.22	66.69	
B	3797.58	Low-Fe calcite	-0.55	-8.73	63.45	
A	3432	Ferroan calcite	-6.85	-12.66		113.64
A	3637	Ferroan calcite	-8.79	-12.82		115.38
A	3635	Ferroan calcite	-9.03	-14.29		132.19
B	3799.66	Ferroan calcite	-8.86	-15.87		152.98
B	3804.08	Ferroan calcite	-6.43	-15.09		142.23
D	3884	Ferroan calcite	-11.01	-16.39		160.44
C	3304	Ankerite	-9.76	-13.87		127.12
C	3312	Ankerite	-9.25	-15.17		143.40
C	3319	Ankerite	-7.81	-15.08		142.21
A	3530	Ankerite	-9.69	-16.63		164.09
A	3548	Ankerite	-10.87	-17.25		173.98
E	3931	Ankerite	-11.34	-15.65		149.84
E	3940	Ankerite	-12.39	-16.86		167.75

$\delta^{13}C_{PD}$  values of ferroan calcite cements vary from  $-11.00\text{‰}$  to  $-6.43\text{‰}$  and  $\delta^{18}O_{PDB}$  values range from  $-16.39\text{‰}$  to  $-12.66\text{‰}$  (Figure 9 and Table 2).  $\delta^{13}C_{PDB}$  values of ankerite vary from  $-12.39\text{‰}$  to  $-7.81\text{‰}$  and  $\delta^{18}O_{PDB}$  values range from  $-17.25\text{‰}$  to  $-13.87\text{‰}$  (Figure 9 and Table 2).

## 5. Discussion

### 5.1. Paragenetic Sequence

Based on the petrographic observations combined with mineral geochemistry and burial history, the paragenetic sequence of the main diagenetic events has been established (Figure 10).

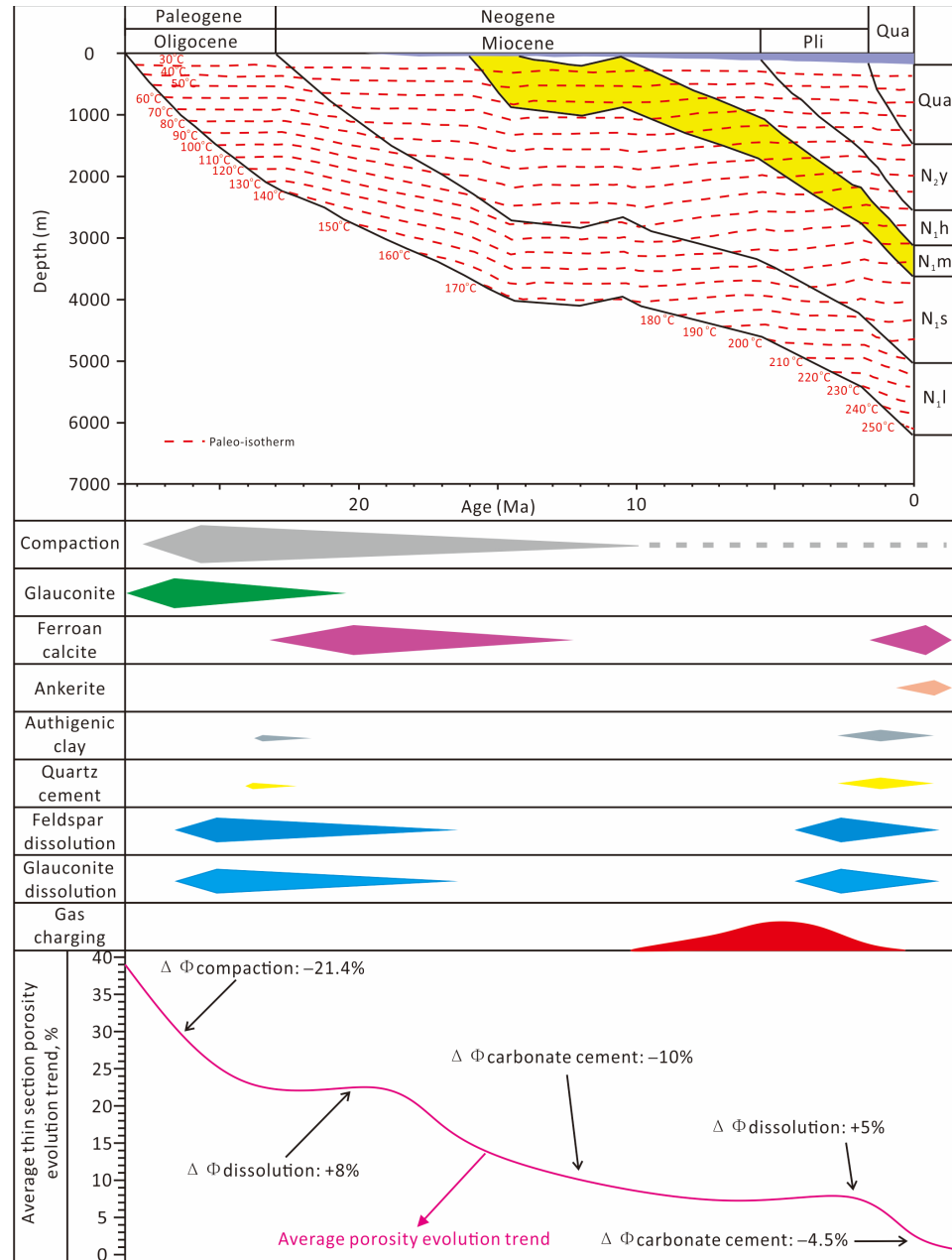


**Figure 10.** Burial, thermal, diagenetic history, and average thin-section porosity evolution trend of the N1m sandstone reservoirs. The width of the symbols represents the relative occurring rate of authigenic minerals and oil charging.

#### 5.1.1. Eogenesis

Eogenesis usually occurs at temperatures below 70.00 °C [30], which is comparable to a burial depth of about 1 km in the studied sandstone (Figure 10). In the shallow burial process, mineralization is significantly affected by the composition of the parent rock and the geochemical characteristics of ambient pore fluids during shallow burial environ-

ments [31]. Eogenetic processes in the N<sub>1</sub>m interval mainly include mechanical compaction, precipitation of glauconite and calcite, as well as the dissolution of feldspar (Figure 10).

Glauconite is a kind of mineral rich in Fe, Mg, and K, which is a typical marine authigenic mineral [32,33]. The glauconite in the N<sub>1</sub>m sandstones mainly occurs as spherical glauconite (Figure 6D). Authigenic glauconite is slowly fused by discrete tiny patches in the early stage to form a symbiotic glauconite particle with a skeleton particle [34,35]. Glauconite is usually transported by water after in situ precipitation, and is reworked with detrital grains under mechanical depositional differentiation [36,37]. The roundness of glauconite is good in the study samples, indicating that it has undergone short distance transport. Moreover, most glauconite is deformed by mechanical compaction (Figure 6D), so the formation of glauconite cement is earlier than the early compaction.

The N<sub>1</sub>m sequences experienced a short subsidence in the initial deposition prior to the early tectonic uplift (Figure 10). Subsequently, the N<sub>1</sub>m sequence is uplifted to the near earth surface during the early tectonic uplift between 12 and 10 Ma (Figure 10). This tectonic process would lead to the intrusion of meteoric water and result in the early dissolution of feldspar minerals. Dissolved pore of feldspar infilled with low-Fe calcite cement indicates that feldspar dissolution is predated on precipitation of low-Fe calcite (Figure 8F). The evidence of casting thin sections showed the extensive dissolution of feldspar grains in sandstone samples with a large amount of ferroan calcite cementation (Figure 8D–F). The precipitation temperature of carbonate cementation can be calculated by stable oxygen isotope, and the  $\delta^{18}\text{O}_{\text{SMOW}}$  value of seawater at that time is about 0‰ in the Qiongdongnan Basin [38]. Based on the oxygen isotope fractionation equations for calcite water [39], the calculated precipitation temperatures of low-Fe calcite ranged from 54.1–66.7 °C, with an average value of 60.4 °C (Table 2).

$$1000 \ln \alpha_{\text{Ca-H}_2\text{O}} = 2.78 \times 10^6 / T^2 - 2.89 \quad (1)$$

Carbonate cements have various sources, including internal, external, and mixed sources [40,41]. The internal sources are mainly derived from dissolution of detrital and biogenic carbonate fragments [42,43], while the external sources are a result of the diffusive transport of ions from adjacent mudstones [40,44].

The presence of framboidal pyrite confirms the bacterial sulfate reduction occurred and framboidal pyrite is typically a by-product of bacterial sulfate reduction (Figure 7F; [45]). The cross-plot of the carbon versus oxygen isotope indicates that the carbon sources of low-Fe calcite cements are mainly derived from bacterial sulfate reduction from adjacent mudstones (Figure 9; [46]). The low-Fe calcite commonly occurring at the interface between sandstone and mudstone (Figure 6E) also supports this inference. As described above, foraminifer shell fragments are commonly identified in the N<sub>1</sub>m sandstone (Figure 8B,C). The dissolution of foraminifera in the sandstones can provide abundant  $\text{HCO}_3^-$  and  $\text{Ca}^{2+}$  ions [47,48], which is beneficial for the formation of large amounts of low-Fe calcite cements. Therefore, based on the petrographic observation coupled with mineral geochemistry, it is inferred that the low-Fe calcites are mainly derived from the bacterial sulfate reduction from adjacent mudstones and the dissolution of interval foraminifer shells in the sandstones.

### 5.1.2. Mesogenesis

Diagenetic products during mesogenesis include the dissolution of feldspar, precipitation of ferroan calcite and ankerite, quartz and authigenic clays. At increasing temperatures and pressures, the organic matter of the underlying Oligocene Yacheng source rocks experienced a thermal maturity stage, releasing large amounts of organic acids and  $\text{CO}_2$  [49]. The intrusion of organic fluids into the N<sub>1</sub>m sandstones leads to the dissolution of unstable feldspar minerals which is closely associated with quartz cements and authigenic clays (Figure 7C–E).

Petrographic evidence from isolated ferroan calcite and ankerite cements indicates that they precipitated after significant mechanical compaction. The content of the late-staged ferroan carbonates dose not change with the distance from the contact surface

of sandstone and mudstone (Figures 6F and 7A). Stable carbon isotopes can be used to identify the carbon source of carbonate cements [50]. Carbon isotopes of the ferroan calcite ( $\delta^{13}\text{CPDB}$ :  $-11.00\text{‰}$  to  $-6.43\text{‰}$ ) and ankerite ( $\delta^{13}\text{CPDB}$ :  $-12.39\text{‰}$  to  $-7.81\text{‰}$ ) indicate that the carbon sources of cements are mainly derived from organic matter decarboxylation (Table 2 and Figure 9). After the organic matter is mature in mudstone, a large amount of organic  $\text{CO}_2$  will be released after thermal decarboxylation. Therefore, the formation of ferroan calcite and ankerite are related to the decarboxylation of organic matter, and may inherit some carbon sources from early-formed low-Fe calcite in the sandstones. Moreover, glauconite alteration during diagenesis could provide Fe and Mg ions for ferroan calcite and ankerite cementation (Figure 11).

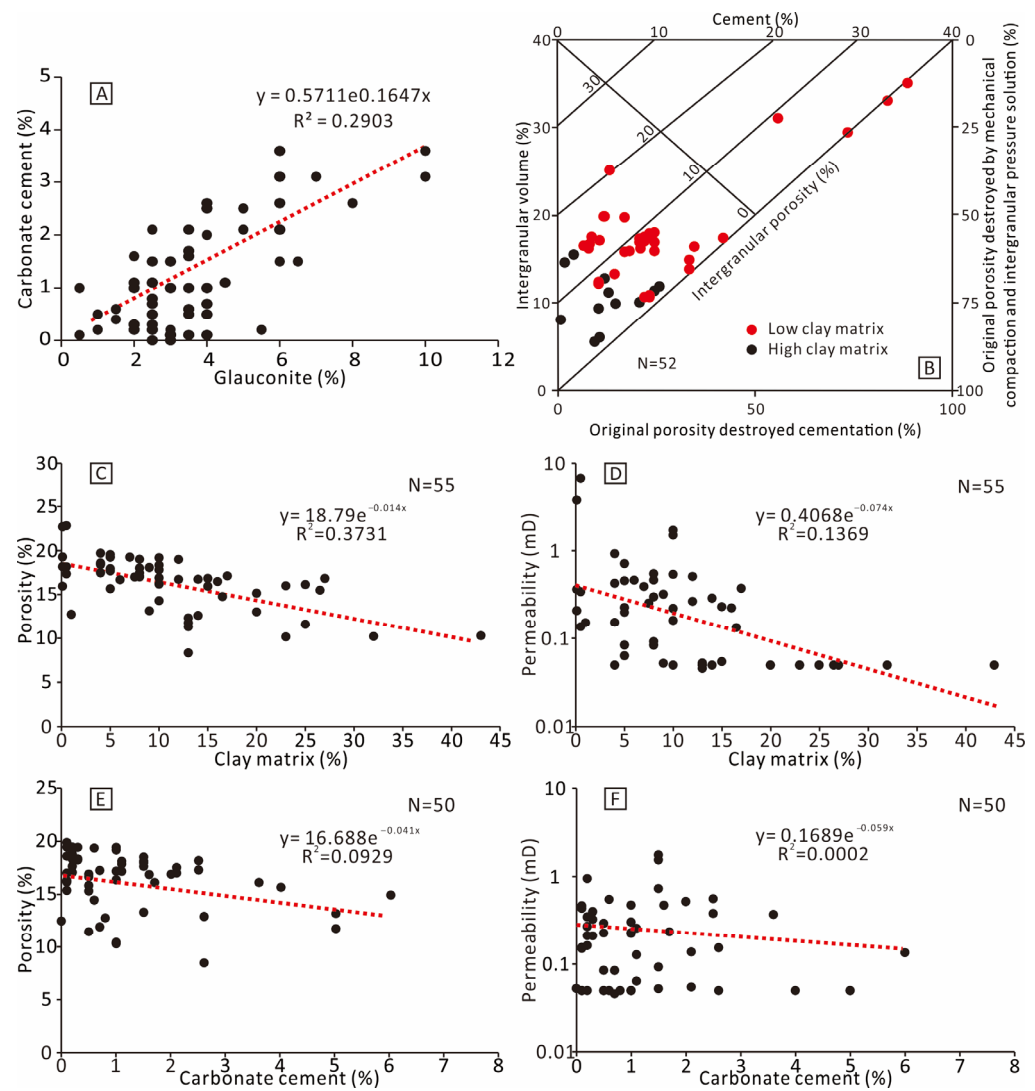


**Figure 11.** (A) Cross-plots of the relationships between the content of glauconite and later-staged ferroan carbonates. (B) A plot of intergranular volume against cement volume. Cross-plots of the relationships between the content of clay matrix and (C) porosity and (D) permeability, between the content of carbonate cement and (E) porosity and (F) permeability.

The  $\delta^{18}\text{OSMOW}$  values of pore fluids from which ferroan carbonate precipitated is estimated to be  $4\text{‰}$ . Based on the oxygen isotope fractionation equations for calcite water (1) [51], calculated precipitation temperatures of ferroan calcite ranged from  $113.64\text{--}160.44\text{ °C}$ , with an average value of  $136.14\text{ °C}$  (Table 2). Based on the oxygen isotope fractionation equations for ankerite-water (2) [52], calculated precipitation temperatures of ankerite ranged from  $127.12\text{--}173.98\text{ °C}$ , with an average value of  $152.62\text{ °C}$  (Table 2). Compared

with the calculated temperature results of gas charging, the start of oil emplacement was prior to the onset of carbonate cementation (Figure 11 and Table 2).

$$1000 \ln \alpha_{D-H_2O} = 3.06 \times 10^6 T^{-2} - 3.24 b \quad (2)$$

### 5.2. Origin of Overpressure

Representative Well A in the studied area is located in the deep overpressure section (3600.00–3640.00 m) of Meishan Formation (Figure 12A). The abnormal high interval transit time (Figure 12B) in this section corresponds to the decrease in density and resistivity (Figure 12C,D), which may indicate the existence of disequilibrium compaction. In addition, it can be seen from the burial history map that the formation of Meishan Formation has a very fast subsidence rate (Figure 10), and in the formation, there is a large set of mudstone with thin-layer sandstones (Figure 12A). It is concluded that this rapid burial and high proportion of mudstone may also promote the disequilibrium compaction overpressure of the formation.

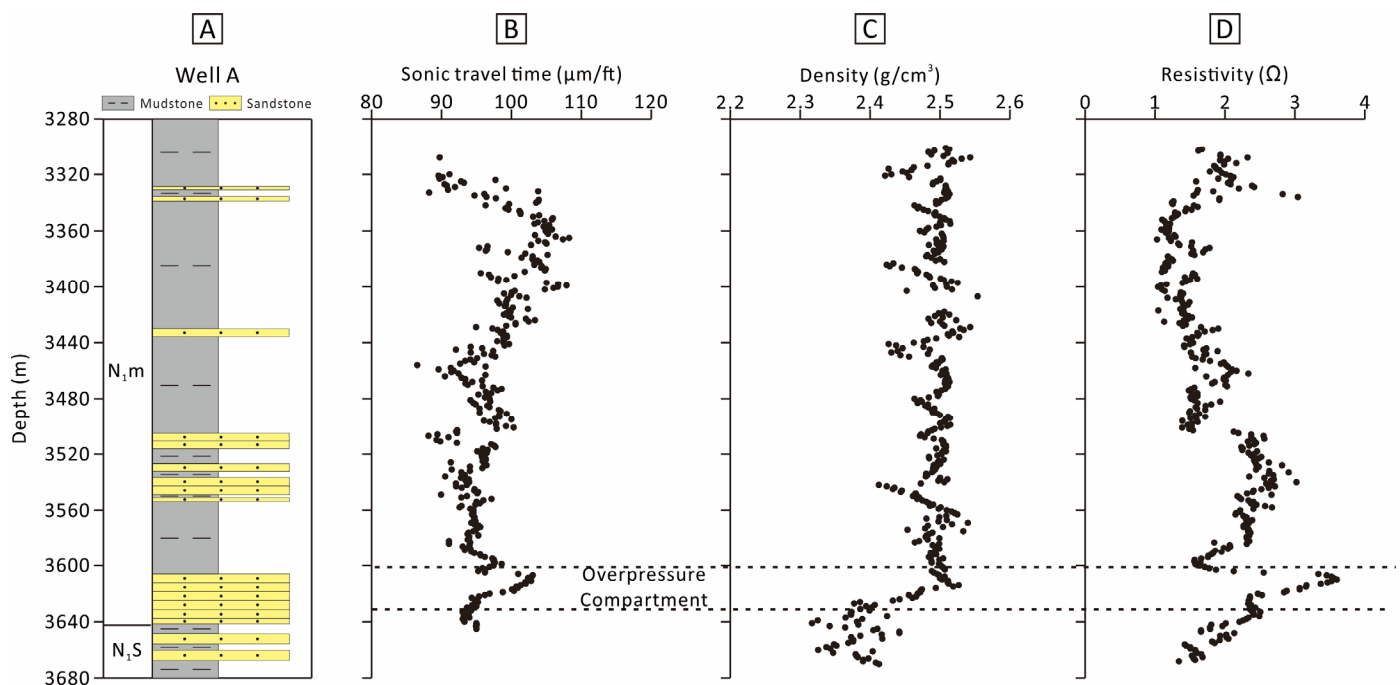


**Figure 12.** Lithologic column (A), sonic travel time (B), density (C), and resistivity (D) in Well A in the Ledong–Lingshui Sag.

A large number of two-phase aqueous inclusions which were trapped simultaneously with a migration of natural gas were identified in quartz fractures. The microthermometry results show that the homogenization temperature of aqueous inclusions ranges from 117.60 to 179.60 °C with an average of 144.10 °C, which confirms the charging time of natural gas (Figure 13). According to the interval transit time-density chart [53], the genetic mechanism of overpressure in Well D was determined. In normally compacted sedimentary strata, as the vertical effective stress acting on the sediment continues to increase, the density of the sediment increases and the interval transit time decreases, so a positive correlation is shown on the graph, which is called the loading curve [54] (Figure 14). The overpressure caused by the disequilibrium compaction is generally expressed as the increase in interval transit time and the decrease in density (Figure 14). Therefore, it is determined that the mechanism of the first overpressure is disequilibrium compaction overpressure. The overpressure caused by hydrocarbon generation expansion shows an increase in interval transit time and a constant or slight decrease in density curve value on the logging curve (Figure 14). Combined with the hydrocarbon generation capacity of the rock in the well, whether the

source rock has entered the natural gas window can be judged according to the Ro value of kerogen in the high-pressure area. It can be seen that the depth corresponding to the peak of Ro is basically the same as the depth of the high pressure region [55]. Therefore, it is concluded that the mechanism leading to the second overpressure in the deep depth of the study area may be hydrocarbon generation pressurization.

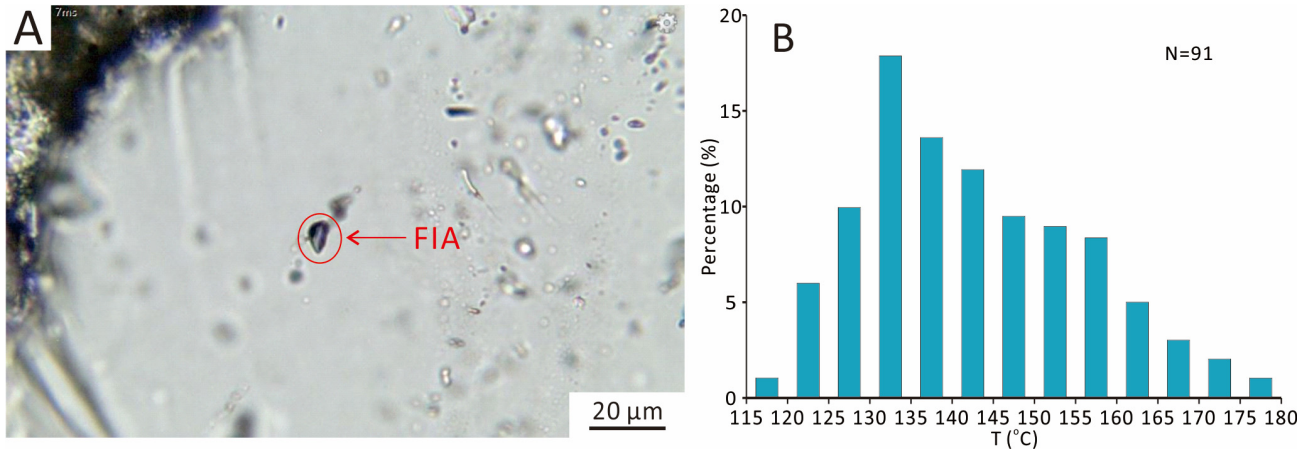


**Figure 13.** (A) Photomicrographs of aqueous inclusions in quartz. (B) Comparison of the homogenization temperatures of the aqueous inclusions in hydrocarbon inclusions. AI = aqueous inclusion.

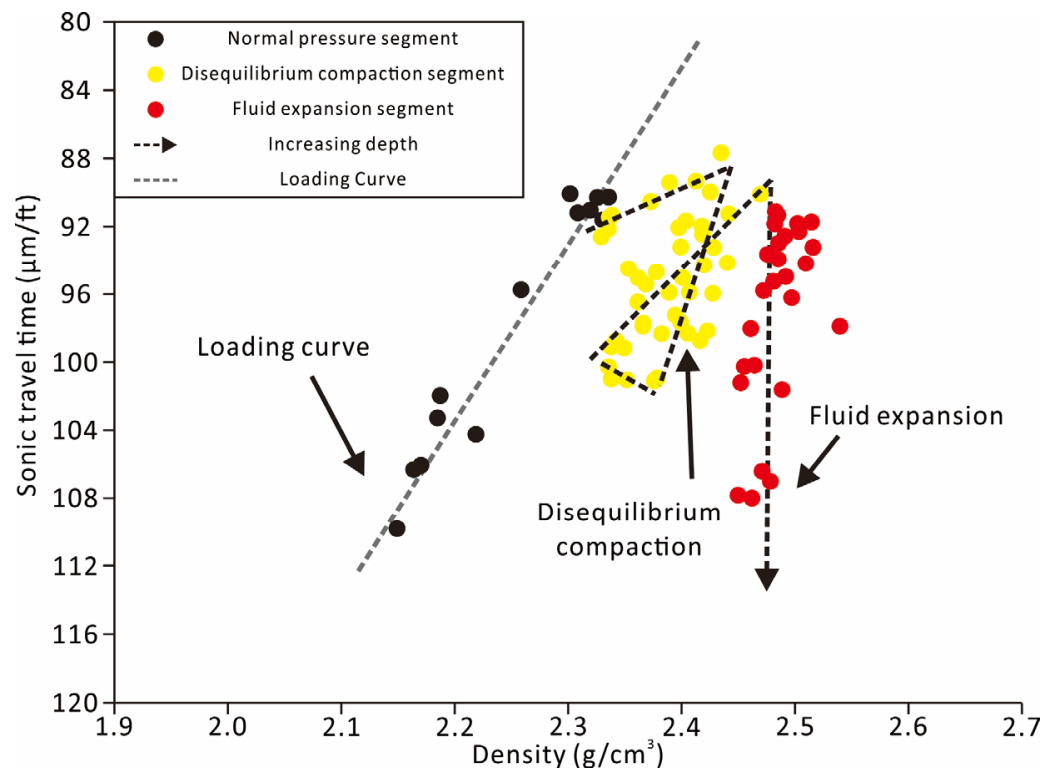


**Figure 14.** The cross-plot between sonic travel time and density of mudstone in Well D.

### 5.3. Diagenetic Controls on Reservoir Quality

Reservoir quality and heterogeneity are affected by a sedimentary environment, sedimentary fabric, diagenesis, hydrocarbon filling, deep hydrothermal, abnormal pressure, and other factors [56,57]. In the N1m sandstones, the grain size and sorted coefficient have not changed much. Therefore, the reservoir quality is controlled by sedimentary fabric and diagenesis. Different types of diagenesis affect the pore characteristics of the reservoir, thereby affecting the quality of the reservoir [58,59].

Mechanical compaction is an important diagenesis in the process of the burial diagenesis of sandstone reservoirs, which usually destroys the primary pore space of sandstone, and is one of the most important mechanisms to reduce the quality of sandstone reservoir [60,61]. Buried depth is the main factor affecting mechanical compaction [62]. The maximum buried depth of N1m sandstone is about 4000 m in the study area, and the quartz grains show line contact to concave and convex contact (Figure 6B), and the ductile grains such as mica are bent and deformed by mechanical compaction (Figure 6A). The effect of mechanical compaction on the reservoir can be assessed by calculating the intergranular volume (IGV), defined as the sum of the clastic matrix, intergranular cement, and intergranular porosity. The IGV abundance is 5.70%–25.50%, with an average of 14.60%. The variation of interparticle volume may be related to the clay matrix and unstable plastic grains. The mechanical compaction is greatly affected by the original sedimentary fabric, and has a wide range of compaction characteristics with a high content of clay matrix in sandstone samples (Figure 6C). A negative correlation can be observed between the clay matrix content and the physical properties of the analyzed sandstones (Figure 11B–D), indicating that clay matrix has a destructive impact on reservoir quality. This is because the original porosity of this kind of sandstone is low, and the existence of clay matrix promotes the compaction, leading to the rapid depletion of porosity. The effect of compaction with a low content of clay matrix is small on sandstone samples, because of the existence of rigid grains, it can resist the pressure of overlying strata.

Cementation also played a major role in reducing porosity and permeability in the studied sandstone reservoirs [60], even though mechanical compaction is volumetrically the most important. The most abundant pore-occluding cement types recognized in this study are carbonate. The different types of cement occlude both pores and pore throats, making the reservoir quality extremely poor.

In the studied area, the carbonate cement is mainly composed of ferroan calcite. Early ferroan calcite mainly developed in the alkaline pore water environment, showing extensive cementation (Figure 6E), and this kind of carbonate caused the rapid depletion of reservoir porosity. Late calcite is usually scattered in the pore space, which will also reduce the reservoir quality (Figures 6F and 7A). The content of calcite cement is negatively correlated with the porosity and permeability of sandstone (Figure 11E,F). Therefore, whether the formation time of carbonate cement is early or late, the reservoir quality will be affected, and the high content of carbonate cement is not conducive to the formation of high-quality reservoirs.

Dissolution is an important mechanism for improving the reservoir quality of sandstone [63,64]. In the eogenesis, the leaching of meteoric water led to the extensive dissolution of feldspar grains, forming a small number of secondary pores (Figure 8D,F). At elevated temperatures, abundant organic acids and CO<sub>2</sub> were released during mesogenesis resulting in the continuous dissolution of feldspar grains in the sandstone reservoirs, forming a large number of secondary pores (Figure 7C,D and Figure 8E). Two stages of mineral dissolution would greatly enhance reservoir porosity and permeability.

#### *5.4. Implications for High-Temperature and High-Pressure Reservoir Exploration*

The significance of this study is to discuss the diagenetic evolution and its influence on reservoir quality under the background of high temperature and pressure in the deep-water, deep-buried regimes. The physical properties of deep-water siliciclastic reservoirs are controlled by the original sedimentary fabric, but the late diagenetic transformation also affects the evolution of the reservoirs [65].

The early disequilibrium compaction and natural gas charging time are the main mechanism of overpressure formation, and are important factors affecting the reservoir quality. The early overpressure can more strongly inhibit mechanical compaction, and even in the deep-buried environment, there is point contact between the debris particles. Therefore, it can be concluded that the early overpressure can effectively maintain the initial intergranular volume of the sandstone. Late overpressure can resist mechanical compaction

and protect the pore structure continuously. Both early and late overpressure affect the pore structure of the reservoir. Although mechanical compaction generally exists in deep-buried sandstone, it is greatly influenced by the original depositional framework composition. Thin-bedded sandstones and the bottom section of the thick-bedded sandstones are characterized by extensive mechanical compaction due to poor-sorted, high clay matrix content (Figure 6C), and this process results in low initial porosity. In the eogenetic and mesogenetic alterations, mechanical compaction is promoted and the original intergranular volume is significantly destroyed. Thus, dissolution is difficult to occur, and overpressure cannot provide effective protection in the thin-bedded sandstones and the bottom section of the thick-bedded sandstones (Figures 15 and 16A). Reservoirs with good physical properties preferentially develop in the middle section of the thick-bedded sandstones, which commonly have high initial porosity owing to relatively well-sorted, low clay matrix contents. In the diagenetic process, extensive feldspar grains were dissolved and a large number of secondary pores were formed (Figure 8E). The early disequilibrium compaction and natural gas charging make overpressure generally develop, and the formation of overpressure can effectively resist the overlying formation pressure (Figures 12 and 14). However, after diagenetic transformation, sandstone with a good original depositional framework composition and sorted content still retains a large number of primary and secondary pores (Figure 5C,D), which can be effectively protected by overpressure, and makes an important contribution to the formation of abnormally high primary and secondary pore zones (Figures 15 and 16B). Extensive carbonate cementation usually occurs at or near sandstone–mudstone contacts (Figure 6E). Multiple generations of carbonate cementation continued to destroy the pore structure, resulting in low porosity (Figures 15 and 16C). In summary, original depositional framework composition had a critical control on diagenetic reactions, which in turn dictated reservoir quality in the N1m interval.

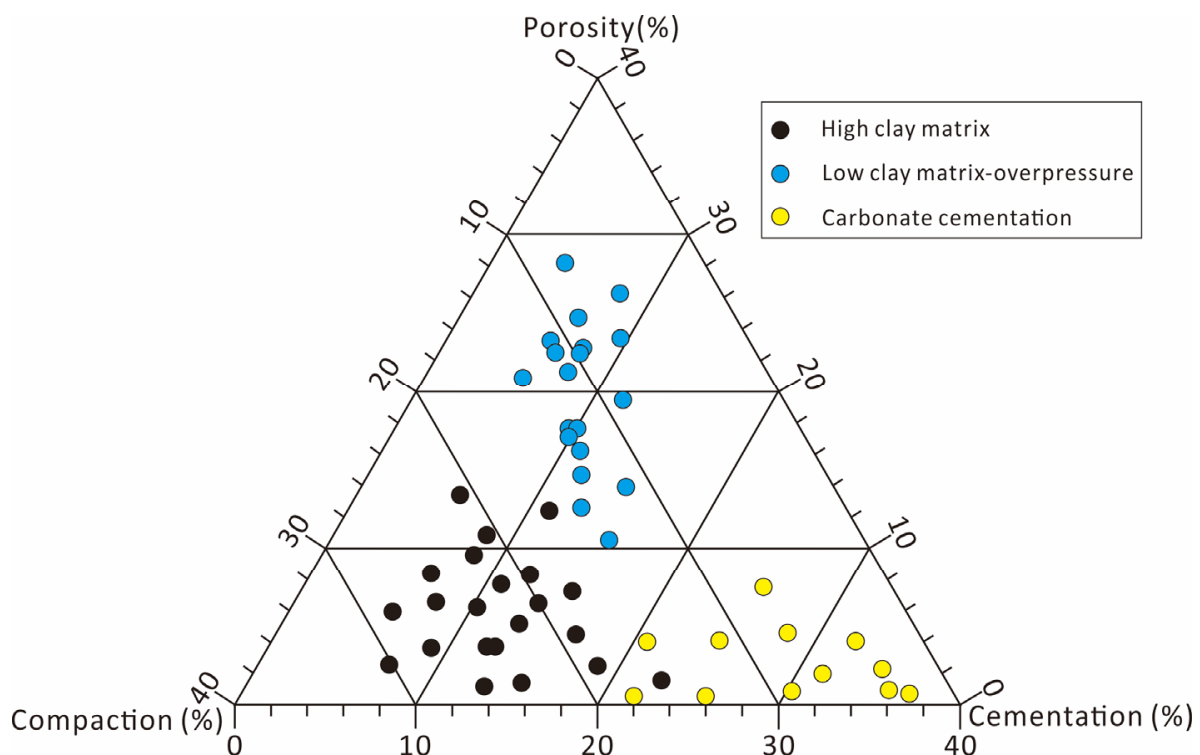


**Figure 15.** Ternary plot of plug porosity, porosity destroyed by mechanical compaction and volumes of authigenic cements.

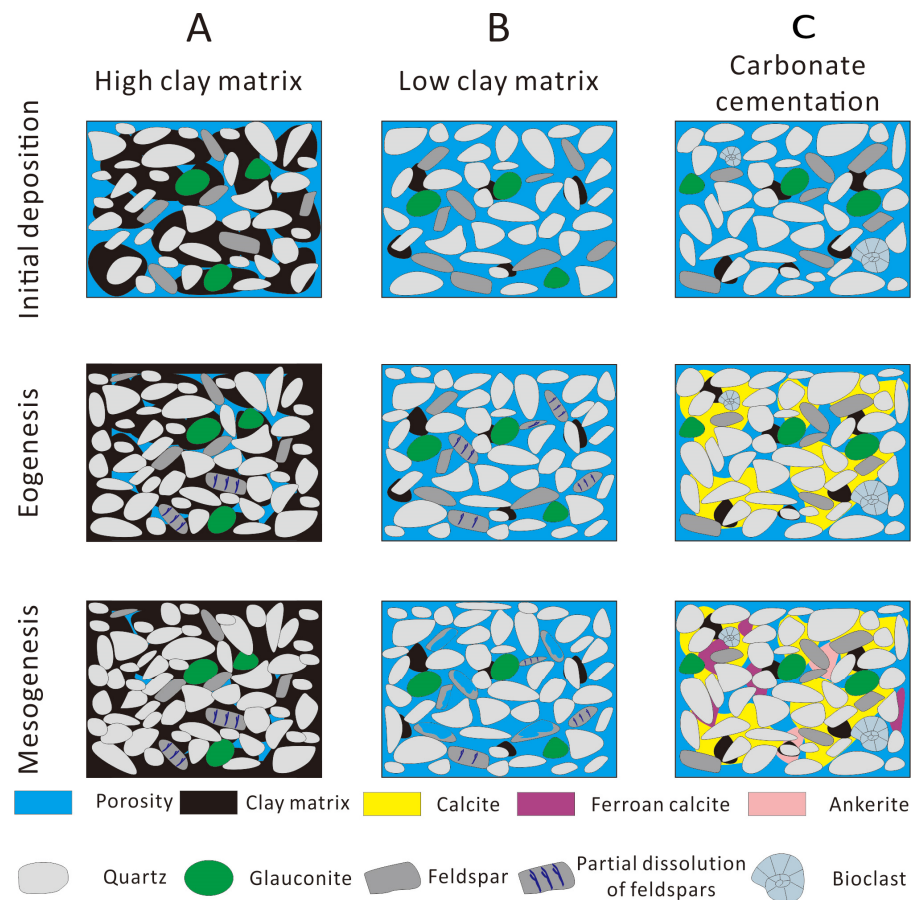


**Figure 16.** Schematic diagram showing typical diagenetic alterations and related reservoir evolution pathways for the N1m sandstones. (A) = Sandstone with high clay matrix content. (B) = Sandstone with low clay matrix content. (C) = Carbonate cemented sandstone.

## 6. Conclusions

Based on the integration of depositional framework composition, diagenetic modifications, and burial history evolution, this study investigates the diagenesis of N<sub>1</sub>m sandstone reservoir and its impact on reservoir quality under the background of HTHP deep-buried sandstones. The conclusions are described as follows:

1. Eogenetic processes in the Neogene N<sub>1</sub>m interval included mechanical compaction, dissolution of feldspar and low-Fe calcite cementation. Typical mesodiagenetic processes included dissolution of feldspar, high-Fe ferroan calcite and ankerite formation, and precipitation of quartz and clay mineral.
2. Original depositional framework composition critically influenced eogenetic and mesogenetic reactions which, in turn, directly dictated the reservoir quality. Extensive mechanical compaction commonly occurs in thin-bedded sandstones and the bottom section of the thick-bedded sandstones, due to their poor-sorted and high clay matrix content. Due to good original depositional framework composition in the middle section of the thick-bedded sandstones, the initial porosity is high and the feldspar grains are extensively dissolved, resulting in good reservoir quality. Extensive carbonate cementation develops at or near the sandstone–mudstone contacts, which results in the serious destruction of pore structure.
3. The formation of overpressure is induced by early disequilibrium compaction and subsequent natural gas charging. Relatively well-sorted sandstones underwent multiple stages of diagenetic alteration, resulting in the development of a large number of primary and secondary pores. The formation of overpressure resisted the pressure of the overlying strata, effectively protects reservoir porosity, and thus, leads to different

development zones of abnormally high porosity in the deep-buried environments. However, the sandstones with a poor original depositional framework composition experienced strong mechanical compaction, and it is difficult to undergo dissolution alteration in the subsequent diagenesis, and overpressure cannot provide effective protection for reservoir porosity.

4. Deep-water sandstones are pervasively developed worldwide and have received much more attention for geologists; therefore, the findings of this study have wide application to reveal the origin of high-quality reservoirs in the HTHP deep-buried sandstones. A better understanding of complicated diagenetic alterations would improve predictive reservoir models of deep-water, deep-buried sandstones of similar origins.

**Author Contributions:** Conceptualization, L.H. and B.M.; methodology, B.M.; software, L.H.; validation, L.H., W.L. and B.M.; formal analysis, L.H.; investigation, L.H.; resources, L.H.; data curation, W.L.; writing—original draft preparation, B.M.; writing—review and editing, B.M.; visualization, B.M.; supervision, B.M.; project administration, L.H.; funding acquisition, L.H. All authors have read and agreed to the published version of the manuscript.

**Funding:** This study was financially supported by the scientific and technological project of the China National Offshore Oil Corporation (CNOOC) (No. KJ135ZDXM38ZJ02ZJ, No. KJGG2022-0102).

**Data Availability Statement:** Data are contained within the article.

**Acknowledgments:** We are grateful to the Haikou Research Institute of the China National Offshore Oil Corporation for providing data used in this study and the permission to publish the results.

**Conflicts of Interest:** Lin Hu and Wei Luo was employed by Hainan Branch of CNOOC Limited, Haikou 570100, China. The remaining authors declare that the research was conducted in the absence of any commercial or financial relationships that could be construed as a potential conflict of interest.

## References

1. Dou, L.R.; Wen, Z.X.; Wang, J.J.; Wang, Z.M.; He, Z.J.; Liu, X.B.; Zhang, N.N. Analysis of the world oil and gas exploration situation in 2021. *Pet. Explor. Dev.* **2022**, *49*, 1195–1209. [\[CrossRef\]](#)
2. Wen, Z.X.; Wang, J.J.; Wang, Z.M.; He, Z.J.; Song, C.P.; Liu, X.B.; Zhang, N.N.; Ji, T.Y. Analysis of the world deepwater oil and gas exploration situation. *Pet. Explor. Dev.* **2023**, *505*, 1060–1076. [\[CrossRef\]](#)
3. Gao, Y.; Qu, X.Y.; Yang, X.B.; You, L.; Zhong, J.; Dong, X.F.; Cao, Y.Q.; Wang, Y.P. Characteristics of fluid inclusions and accumulation period of Miocene reservoir in ledong-lingshui sag of Qiongdongnan Basin. *China Offshore Oil Gas* **2018**, *23*, 83–87.
4. Zhao, N.; Wang, L.; Zhang, W.; Peng, Y.C.; Sima, L. Investigation of pore structure characteristics in marine deep-water high-temperature and high-pressure sandstone: A comprehensive characterization combining various experimental techniques. *Geoenergy Sci. Eng.* **2023**, *222*, 211433. [\[CrossRef\]](#)
5. Xie, Y.H. A major breakthrough in deepwater natural gas exploration in a self-run oil/gas field in the northern South China Sea and its enlightenment. *Nat. Gas Ind.* **2014**, *7*, 30–39.
6. Gao, Y. Characteristics of Thermo-Pressure Environment and Its Influence on Reservoirs in L Sag, Qiongdongnan Basin. Master's Thesis, China University of Petroleum, Beijing, China, 2020.
7. Lin, Y.C. Miocene Reservoir Characteristics and Genesis of High-Quality Reservoirs in L Sag, Qiongdongnan Basin. Master's Thesis, China University of Petroleum, Beijing, China, 2020.
8. Shi, H.S.; Zhu, J.Z.; Jiang, Z.L.; Shu, Y.; Xie, J.T.; Wu, J.Y. Re-evaluation of oil and gas resources in Zhuyi Depression, Pearl River Estuary Basin. *China Offshore Oil Gas* **2009**, *21*, 9–14.
9. Shao, L.; Li, A.; Wu, G.X.; Li, Q.Y.; Liu, C.L.; Qiao, P.J. Sedimentary environment and provenance evolution in Qiongdongnan Basin. *Acta Pet. Sin.* **2010**, *31*, 548–552.
10. Li, D.W.; Li, D.S.; Chen, C.M. Overview of deep-sea fan oil and gas exploration. *China Offshore Oil Gas* **2007**, *24*, 18–24.
11. Deng, R.J.; Deng, Y.H.; Yu, S.; Hou, D.J. Petroleum geology and accumulation characteristics in the Niger Delta Basin. *Pet. Explor. Dev.* **2008**, *35*, 755–762.
12. Jamil, M.; Siddiqui, N.A.; Usman, M. Facies analysis and distribution of Late Palaeogene deep-water massive sandstones in submarine-fan lobes, NW Borneo. *Geol. J.* **2022**, *57*, 4489–4507. [\[CrossRef\]](#)
13. Zhang, J.J.; Wu, S.H.; Hu, G.Y.; Fan, T.E.; Lin, P. Application of four-dimensional monitoring to understand reservoir heterogeneity controls on fluid flow during the development of a submarine channel system. *Am. Assoc. Pet. Geol. Bull.* **2018**, *102*, 2017–2044. [\[CrossRef\]](#)
14. Navarro, L.; Arnott, R.W.C. Stratigraphic record in the transition from basin floor to continental slopeseimentation in an ancient passive-margin Windermere turbidite system. *Sedimentology* **2019**, *67*, 12676.

15. Wang, Z.F.; Sun, Z.P.; Zhang, Y.Z.; Guo, M.G.; Zhu, J.T.; Huang, B.J. Distribution and hydrocarbon accumulation mechanism of the giant deepwater Central Canyon gas field in Qiongdongnan Basin, northern South China Sea. *China Pet. Explor.* **2016**, *21*, 54–56.
16. Su, A.; Chen, H.H.; Chen, X.; Liu, H.B.; Liu, Y.H.; Lei, M.Z. New insight into origin, accumulation and escape of natural gas in the Songdong and Baodao regions in the eastern Qiongdongnan basin, South China Sea. *J. Nat. Gas Sci. Eng.* **2018**, *52*, 467–483. [[CrossRef](#)]
17. Zhang, Y.Z.; Xu, X.D.; Gan, J. Study on the geological characteristics, accumulation model and exploration direction of giant deepwater gas field in the Qiongdongnan Basin. *Acta Geol. Sin.* **2017**, *91*, 1620–1633.
18. Wang, Z.F.; Li, X.S.; Sun, Z.P. Hydrocarbon accumulation conditions and exploration potential in the deep-water region, Qiongdongnan basin. *China Offshore Oil Gas* **2011**, *23*, 7–13.
19. Chen, H.Y. Regional Stratigraphic Framework Establishment and Oil and Gas Accumulation Analysis in Qiongdongnan Basin. Master's Thesis, Ocean University of China, Qingdao, China, 2016.
20. Zhang, Y.X.; Zhu, X.M.; Zhang, G.C.; Chen, H.Q. Sedimentary characteristics of Oligocene Lingshui Formation in Qiongdongnan Basin, South China Sea. *Nat. Gas Geosci.* **2013**, *24*, 956–964.
21. Wu, Y.K.; Hu, M.Y.; Liu, Z.F. The sedimentary facies and coal measures Basin. *Nat. Gas Geosci.* **2013**, *24*, 582–590.
22. Luo, Q.Y.; Jiao, X.Y.; Liu, K.; Li, A.Q.; Song, P. Identification and sedimentation model of submarine fan of Meishan Formation in Ledong-Lingshui Depression. *Mar. Geol. Quat. Geol.* **2020**, *40*, 90–99.
23. Wang, Y. Source Composition, Hydrocarbon Generation Potential of Source Rocks and Its Control on Hydrocarbon Accumulation in Yingqiong Basin. Master's Thesis, China University of Mining and Technology, Beijing, China, 2018.
24. Wang, Z.S.; Liu, Z.; Sun, Z.P. Early prediction and evaluation of Oligocene source rocks in Ledong-Lingshui Sag, Deep water area, Qiongdongnan. *J. Cent. South Univ. Nat. Sci. Ed.* **2014**, *45*, 876–888.
25. Huang, B.J.; Li, X.S.; Wang, Z.F.; Li, L.; Huang, Y.W. Geochemical characteristics and natural gas potential of source rocks in the deep water area of Qiongdongnan Basin. *China Offshore Oil Gas* **2012**, *24*, 1–7.
26. Fan, C.W.; Li, X.S.; Liu, K.; Tan, J.C.; Peng, S.; Hu, L. Reservoir formation conditions of Miocene lithostratigraphic traps in Ledong and Lingshui depressions, Qiongdongnan Basin. *China Offshore Oil Gas* **2016**, *28*, 53–59.
27. Dickson, J.A. Carbonate identification and genesis as revealed by staining. *J. Sediment. Pet.* **1966**, *36*, 491–505.
28. Schmidt, V.; McDonald, D.A. Texture and recognition of secondary porosity in sandstones. In *Aspects of Diagenesis*; Scholle, P.A., Schluger, P.R., Eds.; SEPM Special Publication: Tulsa, OK, USA, 1979; Volume 26, pp. 209–225.
29. Folk, R.L.; Siedlecka, A. The “schizohaline” environment: Its sedimentary and diagenetic fabrics as exemplified by Late Paleozoic rocks of Bear Island, Svalbard. *Sediment. Geol.* **1974**, *11*, 1–15. [[CrossRef](#)]
30. Morad, S.; Ketzer, J.M.; De Ros, L.F. Spatial and temporal distribution of diagenetic alterations in siliciclastic rocks: Implications for mass transfer in sedimentary basins. *Sedimentology* **2000**, *46*, 95–120. [[CrossRef](#)]
31. Liang, J.Y.; Azmy, K.; Li, K.Y.; Liu, S.B.; Li, L.P.; Zhou, G.; Qiu, Y.C.; Li, W.Z.; He, Y.; Wen, H.G. Petrographic and geochemical characteristics of the Middle–Upper Cambrian Xixiangchi dolomites in the central Sichuan Basin, southwest China. Implications for dolomite origins and dolomitization mechanisms. *Mar. Pet. Geol.* **2023**, *152*, 106215. [[CrossRef](#)]
32. Zhang, Q.; Tian, H.Y.; Radwan, A.E.; Lu, D.L.; Zhang, M.J.; Zhong, K. Mineralogical characteristics and genesis mechanism of glauconite in the meso-neoproterozoic and cambrian strata in north China. *Mar. Pet. Geol.* **2023**, *153*, 106280. [[CrossRef](#)]
33. Środoń, J.; Williams, L.; Szczerba, M.; Zaitseva, T.; Bojanowski, M.; Marciniak-Maliszewska, B.; Kuligiewicz, A.; Starzec, K.; Ciesielska, Z.; Paszkowski, M. Mechanism of late diagenetic alteration of glauconite and implications for geochronology. *Geochim. Cosmochim. Acta* **2023**, *352*, 157–174. [[CrossRef](#)]
34. Zhang, Q.; Zhou, C.; Zhu, S.F. Types and genesis of the Neoproterozoic glauconites, Longshan area, Changping district, Beijing. *Geoenergy Sci. Eng.* **2023**, *222*, 211412. [[CrossRef](#)]
35. Roy Choudhury, T.; Khanolkar, S.; Banerjee, S. Glauconite authigenesis during the warm climatic events of Paleogene: Case studies from shallow marine sections of Western India. *Glob. Planet. Change* **2022**, *214*, 103857. [[CrossRef](#)]
36. Huggett, J.M. Glauconites. In *Encyclopedia of Geology*, 2nd ed.; Academic Press: Cambridge, MA, USA, 2021; pp. 334–340.
37. Starzec, K.; Stadnik, R.; Skiba, M. Origin and paleoenvironmental significance of Al-rich glauconite in the Ediacaran/Cambrian deposits of the Lublin Basin, Poland. *Precambrian Res.* **2023**, *397*, 107165. [[CrossRef](#)]
38. Liu, Y.J.; Wei, J.G.; Li, Y.Y.; Chang, J.Y.; Mian, X.M.; Lu, H.L. Seep dynamics as revealed by authigenic carbonates from the eastern Qiongdongnan Basin, South China Sea. *Mar. Pet. Geol.* **2022**, *142*, 105736. [[CrossRef](#)]
39. Friedman, I.; O'Neil, J.R. Compilation of stable isotope fractionation factors of geochemical interest. *Data Geochem.* **1977**, *440kk*, KK1–KK2.
40. Lin, M.R.; Wan, Y.Z.; Cao, Y.C.; Wang, S.P.; Dong, X.Y. Sources of Ca<sup>2+</sup> in the major carbonate cements in Eocene sandstones and conglomerates: Evidence from Sr isotopes, Sr/Ca ratios, and rare-earth elements. *Mar. Pet. Geol.* **2020**, *120*, 104568.
41. Luan, G.Q.; Azmy, K.; Dong, C.M.; Lin, C.; Shi, C. Fault-controlled carbonate cementation: A case study from Eocene turbidite-delta sandstones (Dongying Depression) and implication for hydrocarbon migration. *Mar. Pet. Geol.* **2021**, *129*, 105000. [[CrossRef](#)]
42. Carvalho, M.V.F.; De Ros, L.F.; Gomes, N.S. Carbonate cementation patterns and diagenetic reservoir facies in the Campos Basin cretaceous turbidites, offshore eastern Brazil. *Mar. Pet. Geol.* **1995**, *12*, 741–758. [[CrossRef](#)]
43. Jurkowska, M.K.S. The role of biogenic silica in the formation of Upper Cretaceous pelagic carbonates and its palaeoecological implications. *Cretac. Res.* **2019**, *93*, 170–187. [[CrossRef](#)]

44. Janssen, M.; Caracciolo, L.; Bonnell, L.M. Climatic, depositional and environmental controls on early carbonate cementation in fluvial and shallow marine sandstones. *Mar. Pet. Geol.* **2023**, *156*, 106433. [[CrossRef](#)]
45. Mansurbeg, H.; Morad, S.; Salem, A.; Marfil, R.; El-Ghali, M.A.K.; Nystuen, J.P.; Caja, M.A.; Amorosi, A.; Garcia, D.; La Iglesia, A. Diagenesis and reservoir quality evolution of Palaeocene deep-water, marine sandstones, the ShetlandFaroës Basin, British continental shelf. *Mar. Pet. Geol.* **2008**, *25*, 514–543. [[CrossRef](#)]
46. Brennan, S.T.; Lowenstein, T.K. The major-ion composition of Silurian seawater. *Geochim. Cosmochim. Acta* **2002**, *66*, 2683–2700. [[CrossRef](#)]
47. Swart, K.A.; Oleynik, S.; Martínez-García, A.; Haug, G.H.; Sigman, D.M. Correlation between the carbon isotopic composition of planktonic foraminifera-bound organic matter and surface water pCO<sub>2</sub> across the equatorial Pacific. *Geochim. Cosmochim. Acta* **2021**, *306*, 281–303. [[CrossRef](#)]
48. Takata, H. eCentral Equatorial Pacific benthic foraminifera during the mid-Brunhes dissolution interval: Ballasting of particulate organic matter by biogenic silica and carbonate. *Quat. Sci. Rev.* **2019**, *210*, 64–79. [[CrossRef](#)]
49. Curiale, J.A.; Curtis, J.B. Organic geochemical applications to the exploration for source rock reservoirs—A review. *J. Unconv. Oil Gas Resour.* **2016**, *13*, 1–31. [[CrossRef](#)]
50. Li, J.; Hu, X.; Garzanti, E. Spatial heterogeneity in carbonate-platform environments and carbon isotope values across the Paleocene–Eocene thermal maximum (Tethys Himalaya, South Tibet). *Glob. Planet. Change* **2022**, *214*, 103853. [[CrossRef](#)]
51. Harrison, A.L.; Schott, J.; Oelkers, E.H.; Maher, K.; Mavromatis, V. Rates of carbon and oxygen isotope exchange between calcite and fluid at chemical equilibrium. *Geochim. Cosmochim. Acta* **2022**, *335*, 369–382. [[CrossRef](#)]
52. Matthews, A.; Katz, A. Oxygen isotope fractionation during the dolomitization of calcium carbonate. *Geochim. Cosmochim. Acta* **1977**, *41*, 1431–1438. [[CrossRef](#)]
53. O'Connor, J. The standard gear oil textbook has been ripped up and rewritten following recent advances in wind turbine technology. *Power Eng. Int.* **2011**, *19*, 34, 36–37.
54. Tingay, M.R.P.; Hillis, R.R.; Swarbrick, R.E.; Morley, C.K.; Damit, A.R. Origin of overpressure and pore-pressure prediction in the Baram province, Brunei. *Am. Assoc. Pet. Geol. Bull.* **2009**, *1*, 51–74. [[CrossRef](#)]
55. Wang, Y. Reservoir types and research significance in the deep water area of Qiongdongnan Basin, South China Sea. *Sediment. Tethys Geol.* **2014**, *34*, 82–87.
56. Jamil, M.; Rahman, A.H.B.A.; Siddiqui, N.A.; Ibrahim, N.A.; Ahmed, N. A contemporary review of sedimentological and stratigraphic framework of the Late Paleogene deep marine sedimentary successions of West Sabah, North-West Borneo. *Bull. Geol. Soc. Malays.* **2020**, *69*, 53–65. [[CrossRef](#)]
57. Ibrahim, Y.; Morozov, V.P.; Sudakov, V.; Idrisov, I.; Kolchugin, A.N. Sedimentary diagenesis and pore characteristics for the reservoir evaluation of Domanik formations (Semiluksk and Mendymk) in the central part of Volga-Ural petroleum province. *Pet. Res.* **2022**, *7*, 32–46. [[CrossRef](#)]
58. Imran, Q.S. Facies Heterogeneity and Lobe Facies Multiscale Analysis of Deep-Marine Sand-Shale Complexity in the West Crocker Formation of Sabah Basin, NW Borneo. *Appl. Sci.* **2021**, *11*, 5513.
59. Zhao, J.; Huang, Z.L.; Fan, C.W. Diagenetic and hydrothermal fluid influence on tight sandstone reservoir quality: Gravity-flow deposits from the Huangliu Formation, Ledong area, Yinggehai Basin, South China Sea. *J. Pet. Sci. Eng.* **2022**, *215*, 1106334. [[CrossRef](#)]
60. Javed, A.; Khan, K.F.; Quasim, M.A. Diagenetic characteristics and their implications on the reservoir potential of Bajocian Sandstone, Jaisalmer Basin, western Rajasthan, India. *Geosyst. Geoenviron.* **2023**, *2*, 100219. [[CrossRef](#)]
61. Dou, W.; Lin, M.; Liu, L. The effect of chlorite rims on reservoir quality in Chang 7 sandstone reservoirs in the Ordos Basin, China. *Mar. Pet. Geol.* **2023**, *158*, 106506. [[CrossRef](#)]
62. Huang, S.; Lin, C.; Zhang, X. Controls of diagenesis on the quality of shallowly buried terrestrial coarse-grained clastic reservoirs: A case study of the Eocene Shahejie Formation in the Damintun Sag, Bohai Bay Basin, Eastern China. *J. Asian Earth Sci.* **2021**, *221*, 104950. [[CrossRef](#)]
63. Zhu, N.; Yao, S.P.; Zhang, Y.X.; Ning, S.; Jia, B.; Zhou, Y.; Zhang, W. Influence of coupled dissolution-precipitation processes on the pore structure, characteristics, and evolution of tight sandstone: A case study in the upper Paleozoic reservoir of Bohai Bay Basin, eastern China. *J. Asian Earth Sci.* **2023**, *262*, 105998. [[CrossRef](#)]
64. Hong, D.D.; Cao, J.; Wu, T.; Dang, S.; Yao, S. Authigenic clay minerals and calcite dissolution influence reservoir quality in tight sandstones: Insights from the central Junggar Basin, NW China. *Energy Geosci.* **2020**, *1*, 8–19. [[CrossRef](#)]
65. Fu, Q.L.; Hu, S.Y.; Xu, Z.H.; Zhao, W.; Zeng, H. Depositional and diagenetic controls on deeply buried Cambrian carbonate reservoirs: Longwangmiao Formation in the Moxi–Gaoshiti area, Sichuan Basin, southwestern China. *Mar. Pet. Geol.* **2020**, *117*, 104318. [[CrossRef](#)]

**Disclaimer/Publisher's Note:** The statements, opinions and data contained in all publications are solely those of the individual author(s) and contributor(s) and not of MDPI and/or the editor(s). MDPI and/or the editor(s) disclaim responsibility for any injury to people or property resulting from any ideas, methods, instructions or products referred to in the content.